Stochastic mechanics of loose boundary particle transport in turbulent flow

Subhasish Dey and Sk Zeeshan Ali

Citation: Physics of Fluids **29**, 055103 (2017); doi: 10.1063/1.4984042
View online: http://dx.doi.org/10.1063/1.4984042
View Table of Contents: http://aip.scitation.org/toc/phf/29/5
Published by the American Institute of Physics

Stochastic mechanics of loose boundary particle transport in turbulent flow

Subhasish Dey[a] and Sk Zeeshan Ali[b]
Department of Civil Engineering, Indian Institute of Technology Kharagpur, 721302 Kharagpur, West Bengal, India

(Received 14 February 2017; accepted 8 May 2017; published online 30 May 2017)

In a turbulent wall shear flow, we explore, for the first time, the stochastic mechanics of loose boundary particle transport, having variable particle protrusions due to various cohesionless particle packing densities. The mean transport probabilities in contact and detachment modes are obtained. The mean transport probabilities in these modes as a function of Shields number (nondimensional fluid induced shear stress at the boundary) for different relative particle sizes (ratio of boundary roughness height to target particle diameter) and shear Reynolds numbers (ratio of fluid inertia to viscous damping) are presented. The transport probability in contact mode increases with an increase in Shields number attaining a peak and then decreases, while that in detachment mode increases monotonically. For the hydraulically transitional and rough flow regimes, the transport probability curves in contact mode for a given relative particle size of greater than or equal to unity attain their peaks corresponding to the averaged critical Shields numbers, from where the transport probability curves in detachment mode initiate. At an inception of particle transport, the mean probabilities in both the modes increase feebly with an increase in shear Reynolds number. Further, for a given particle size, the mean probability in contact mode increases with a decrease in critical Shields number attaining a critical value and then increases. However, the mean probability in detachment mode increases with a decrease in critical Shields number. *Published by AIP Publishing.* [http://dx.doi.org/10.1063/1.4984042]

I. INTRODUCTION

Loose boundary particle transport in turbulent wall shear flow is a key topic of interest in many scientific and engineering disciplines. Due to its immense practical applications in Aeolian and fluvial sediment transport,[1–7] slurry pipelines,[8] and many others,[9–11] this topic dwells in the core contents of classical physics and fluid mechanics. The particle transport in near-boundary region is randomly governed by the localized turbulence,[12–16] while that in far-boundary region is controlled by complex advection mechanism.[17,18] Although a plethora of studies were carried out to grasp the underlying flow physics of near-boundary particle transport,[19–28] it is no way exaggeration to declare that a complete understanding of this phenomenon is still in an embryonic stage. The semi-analytical study on this topic dates back to 1936 due to Shields'[29] pioneering contribution to the inception of rheological transport of particles. The *Shields curve* that represents a curve of critical Shields number Θ_c $[= \tau_{0c}/(\rho_p - \rho_f)gD_p]$ versus shear Reynolds number $\mathcal{R}_*$ $(= u_* k_s/\nu)$ is still in use to determine the critical boundary shear stress τ_{0c} for a given particle size D_p. Here, ρ_p is the mass density of particles, ρ_f is the mass density of fluid, g is the gravitational acceleration, u_* is the shear velocity, k_s is the roughness height, ν is the coefficient of kinematic viscosity of fluid, and subscript c denotes the critical criterion. After Shields,[29] more researchers came up with number of theoretical analyses, based on the deterministic and stochastic approaches, and conducted numerous experiments over a wide range of particle sizes and for different flow regimes.[7] White[12] argued that the inception of loose boundary particle transport is practically governed by the instantaneous boundary shear stress rather than its time-averaged value. He emphasized that even if the time-averaged boundary shear stress is less than its critical value, the instantaneous boundary shear stress can cause particles to be transported. Recently, Ali and Dey[30] put forward a comprehensive deterministic analysis of inception of particle transport in a streamflow. However, this study aims to gain insight into the stochastic processes of loose boundary particle transport driven by a turbulent wall shear flow.

Einstein[2] was the first to envision the particle transport phenomenon as a probability of instantaneous hydrodynamic lift arising from the turbulence to exceed the effective gravity of the particles. However, after the discovery of turbulent bursting phenomenon,[31] the particle transport problem has received a new look. During the intermittent events (ejections and sweeps), the conditional Reynolds shear stresses significantly depart from the time-averaged Reynolds shear stress, and thus, such events strongly contribute to the particle transport process.[13,32] Several studies on stochastic dynamics of near-boundary particle transport were carried out experimentally,[19,21,22,33] analytically,[20,24,34–36] and numerically.[15,37–39] Despite several attempts, an in-depth analysis of the stochastic mechanics of near-boundary particle transport in a generalized sense (having variable particle protrusions due to various packing densities of boundary particles) is still lacking. Importantly, little attention has so far been paid on the

[a] sdey@iitkgp.ac.in
[b] Author to whom correspondence should be addressed: skzeeshanali@iitkgp.ac.in

stochastic mechanics of particle transport in different flow regimes. The measurements revealed that sweeps are predominant at the particle transport in a turbulent flow condition.[32,33] Dey *et al.*[32] reported that for a mobile boundary stream, sweeps contribute approximately 70% to the total Reynolds shear stress. The most provoking turbulence characteristic towards the particle transport can be envisaged as a near-boundary low-pressure field induced by sweeps.[32] Therefore, the inclusion of such an aspect in the mathematical analysis, proper selection of the probability density function (PDF) of near-boundary instantaneous streamwise velocity, is an essential prerequisite. The link between the kurtosis of the PDF and the spectral slope reveals that the PDF of near-boundary instantaneous streamwise velocity has a departure from the Gaussianity.[40] It essentially concludes that the analysis of the particle transport phenomenon can thus be improved by considering a non-Gaussian PDF.

In this study, we explore the turbulent wall shear flow driven cohesionless particle transport from an array of loosely packed boundary particles considering the three-dimensional (3-D) organizations of the particles. The compactness of the boundary particles and their protrusions to the flow are introduced. The analysis is pursued to investigate the particle transport phenomenon in *contact* and *detachment modes* by considering the laws of the wall in hydraulically smooth, transitional, and rough flow regimes. Then, the stochastic analysis of particle transport is introduced from the perspective of the dynamics of near-boundary turbulence structures by applying the *fourth-order Gram-Charlier* probability density function (GC PDF) of the near-boundary instantaneous streamwise velocity. The probabilities of particle transport in contact and detachment modes for various boundary particle conditions are correlated with the fluid induced boundary shear stress. In essence, this study provides a comprehensive understanding of the turbulent wall shear flow driven particle transport in terms of probabilities in contact and detachment modes stemming from the near-boundary turbulence.

The paper is structured as follows. In Sec. II, the physical system under consideration is described. The stochastic analysis of particle transport is presented in Sec. III. The computational results and discussion are furnished in Sec. IV. Finally, the conclusion is drawn in Sec. V.

II. DESCRIPTION OF PHYSICAL SYSTEM

A. Organization of boundary particles

We consider a fully developed unidirectional turbulent shear flow over an array of cohesionless spherical boundary particles of diameter $2r$. The flow has an infinite width and the flow depth is much larger compared to the particle roughness height. The local instantaneous streamwise velocity u is decomposed as $u = \bar{u} + u'$, where an over-bar denotes the time-averaged quantity and a prime denotes the fluctuations. We now pay our attention to a target particle of diameter $2a$ resting on three boundary particles. The roughness height of the boundary particles is taken as $k_s = 2r$. The packing condition of the boundary particles is relaxed indicating that the boundary particles may not be tightly packed [Figs. 1(a) and 1(b)]. In this loosely packed particle organization, the center of

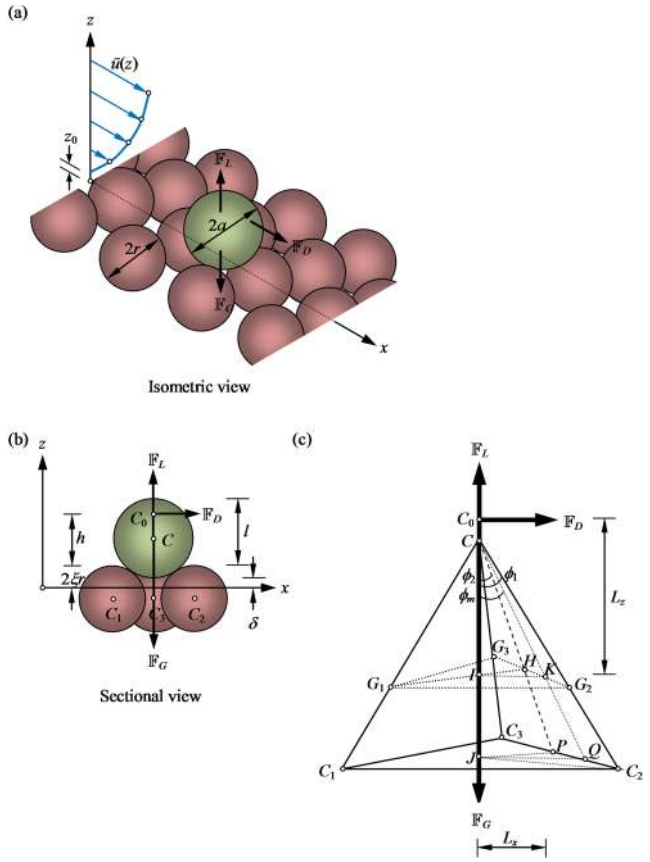

FIG. 1. Schematic of the physical system of a loose boundary: (a) isometric view and velocity field, (b) sectional view and force system, and (c) enlarged view of tetrahedron $CC_1C_2C_3$ and pivoting angles.

the target particle is connected to the centers of the boundary particles to form a tetrahedron $CC_1C_2C_3$, having G_1, G_2, and G_3 as the contact points [Fig. 1(c)]. Note that the effect of the slip at the pivoting points between the particles during the motion of the target particle is absent because the contacts of the particles are considered to be firm due to adequate inter-particle friction. Let us define two key parameters: the protrusion of the target particle l [Fig. 1(b)] and the relative particle size $\mathcal{N}(= r/a)$. For the mathematical treatment, we set the virtual boundary level ($z = 0$) at a vertical distance $2\xi r$ below the summits of the boundary particles. Here, ξ is a proper fraction (<1). The relationship of mean pivoting angle ϕ_m with a, r, and l is derived in Appendix A.

B. Force system

The force system is illustrated in Fig. 1. The instantaneous hydrodynamic drag $\mathbb{F}_D$ and lift $\mathbb{F}_L$ act on the target particle in the streamwise and vertically upward directions, respectively; while, the effective gravity $\mathbb{F}_G$ of the particle acts through its center of gravity vertically downward.

The hydrodynamic drag $\mathbb{F}_D$ comprises of the form drag (that is, the drag induced by the pressure difference p) and skin friction drag (that is, the drag induced by the shear stress τ acting on the surface $\mathcal{S}$ of the particle). Thus, the $\mathbb{F}_D$ is expressed

as

$$\mathbb{F}_D = \int_{\mathcal{S}} (-p\mathbf{n} + \mathbf{n}\tau) \cdot \mathbf{i} d\mathcal{S}. \quad (1)$$

On the other hand, the hydrodynamic lift $\mathbb{F}_L$ is the integral of the pressure forces over the surface $\mathcal{S}$ of the particle. Thus, the $\mathbb{F}_L$ is expressed as

$$\mathbb{F}_L = -\int_{\mathcal{S}} p\mathbf{n} \cdot \mathbf{k} d\mathcal{S}. \quad (2)$$

In Eqs. (1) and (2), $\mathbf{n}$ is the unit vector perpendicular to the $\mathcal{S}$ and $\mathbf{i}$ and $\mathbf{k}$ are the unit vectors along the x- and z-direction, respectively. To calculate these surface integrals, exact expressions for the distributions of pressure and shear stress are the essential prerequisite. However, the evaluation of these surface integrals is not straightforward due to two reasons. First, p and τ are the instantaneous quantities. Second, the description of p and τ becomes uncertain due to the boundary layer separation. Thus, as a first approximation, the drag and lift are expressed as a function of dynamic pressure. It is pertinent to discuss that the development of a more generalized framework for the particle transport phenomenon considering the arbitrary shape, texture, and macro-roughness of particles over a broad spectrum of turbulent flow conditions is a difficult proposition, if not impossible. The difficulties primarily arise from the high intricacy of near-boundary turbulence interaction with the irregular shaped particles, hindering an exceedingly complex analysis of the force system from a micro-mechanistic viewpoint.

The instantaneous drag acting at a distance $z = z_\otimes$ is

$$\mathbb{F}_D = \frac{1}{2} C_D \rho_f u^2_{z=z_\otimes} \mathcal{A}_f, \quad (3)$$

where C_D is the drag coefficient, $u_{z=z_\otimes}$ is the instantaneous streamwise velocity at $z = z_\otimes$, and $\mathcal{A}_f$ is the frontal area (that is, the flow facing area) of the target particle protruding to the flow. The $\mathcal{A}_f$ is considered as the projected area of the target particle above an imaginary plane at $z = 2\xi r$ and is given by $\mathcal{A}_f = (1/4)\{[4\pi a^2 - \cos^{-1}(2l - 2a)] + 4(l - a)[l(2a - l)]^{1/2}\}$. The drag coefficient C_D is a function of particle Reynolds number $\mathcal{R}_p (= 2\bar{u}_{z=z_\otimes} a/\nu)$. Morsi and Alexander[41] studied the response of a spherical particle to a unidirectional flow and extended the Stokes law over a broad spectrum of $\mathcal{R}_p$. They proposed the expression for C_D as $C_D = A_1 + A_2\mathcal{R}_p^{-1} + A_3\mathcal{R}_p^{-2}$, which is used in this study. Here, A_1, A_2, and A_3 are the functions of $\mathcal{R}_p$. The $z_\otimes$ is given by $z_\otimes = 2\xi r + h$, where h is the vertical distance of the point of action of drag from the summits of the boundary particles [Fig. 1(b)]. The h can be obtained by equating the summation of the moment of the distributed drag force with the moment of the resulting drag force about the pivoting point. The lower and upper limits of the distributed force system are considered as $(2\xi r, 2a + \delta)$.

For a simple shear flow with velocity $\mathbf{U}$ having a weak rotation around a stationary spherical particle, Auton[42] showed that Eq. (2) can be expressed as $\mathbb{F}_L = (4\pi a^3/3) C_{LA} \rho_f (\mathbf{U} \times \boldsymbol{\Omega})$, where C_{LA} is the *Auton lift coefficient* and $\boldsymbol{\Omega}$ is the curl of reference velocity at the particle center $(= \boldsymbol{\nabla} \times \mathbf{U})$. However, analogy to the drag, the lift allows us to express the instantaneous lift acting through the center of the target particle as

$$\mathbb{F}_L = \frac{1}{2} C_L \rho_f u^2_{z=z_\otimes} \mathcal{A}_f, \quad (4)$$

where C_L is the lift coefficient. In this study, we performed a sensitivity analysis of C_L (not shown here) by varying it over a certain range. It was found that $C_L = 0.3$ provided the best prediction of the model results.

In addition, the effective gravity of the target particle is expressed as

$$\mathbb{F}_G = \frac{4\pi}{3} a^3 \Delta \rho_f g, \quad (5)$$

where Δ is the submerged relative density of particles $[=(\rho_p - \rho_f)/\rho_f]$.

C. Phenomenology of particle transport

It has been discovered recently that the scaling laws of near-boundary particle transport are inherently linked with the laws of turbulent spectrum.[43] However, in a lucid way, the phenomenology of particle transport can be grasped by setting two distinct transport modes: *contact mode* and *detachment mode*. In contact mode, the target particle has two limits either to roll over the crest of a single boundary particle or to roll over the valley formed by the two neighboring boundary particles. On the other hand, in detachment mode, the instantaneous lift exceeds the effective gravity of the target particle. To better elucidate the transport modes, the time series of $u^2(t)$ is schematically plotted in Fig. 2. Let the contact inception be Q_C and the detachment inception be Q_D. The Q_C and Q_D can be determined from the moment and the force balance of the forces acting on the particle, respectively. In addition to the magnitude of the instantaneous hydrodynamic forces, their durations may also be important to transport the particles as argued by Celik *et al.*[44] They revealed that the impulse triggered by the turbulent flow must exceed the critical impulse value to particle transport. Moreover, the dependency of impulse on the force duration indicated that although the drag is a prerequisite to the particle transport phenomenon, it

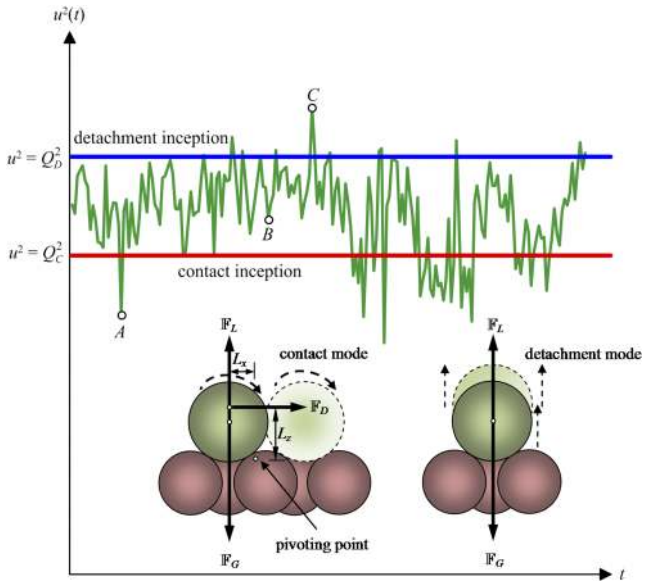

FIG. 2. Conceptual description of contact inception Q_C and detachment inception Q_D in $u^2(t)$ plane.

is not the only motivating force to initiate the particle motion. However, in absence of clear-cut information, the duration of the flow events is not considered here. Further, the instantaneous streamwise velocity is considered as solely responsible for the particle transport rather than the consideration of a more complex situation linked to the burst cycle. Reverting back to Fig. 2, we see that there are three plausible cases. When the magnitude of the instantaneous hydrodynamic forces is considerably small to satisfy the condition $u^2 \in (0, Q_C^2)\ \forall\ \mathcal{R}_*$, that is, the point A in Fig. 2, the target particle cannot completely roll over the pivoting point. However, in this case, the target particle may still have a feeble transport in contact mode remaining within the groove or may remain stationary. For $u^2 \in (Q_C^2, Q_D^2)\ \forall\ \mathcal{R}_*$, that is, the point B in Fig. 2, the particle transports in a pure contact mode keeping in contact to the boundary. On the other hand, for $u^2 \in (Q_D^2, \infty)\ \forall\ \mathcal{R}_*$, that is, the point C in Fig. 2, the transport occurs simultaneously in contact and detachment modes. To be explicit, the third case of transport implies that the particles are lifted off the boundary as they just begin to roll. To determine the Q_C and Q_D, we proceed as follows.

In contact mode, when the target particle is on the verge of rolling, the moment balance about the pivoting point satisfies the criterion $(\mathbb{F}_L - \mathbb{F}_G)L_x + \mathbb{F}_D L_z \geq 0$, where L_x and L_z are the horizontal and the vertical lever arms, respectively. The equality of both the sides in the above criterion represents the inception of particle transport criterion in contact mode, while the inequality signifies the particle transport in contact mode. Substituting Eqs. (3)–(5) into the above criterion yields

$$u_{z=z_\otimes}^2 \geq Q_C^2 = \frac{8\pi a^3 \Delta g L_x}{3\mathcal{A}_f(C_D L_z + C_L L_x)} \forall\ \mathcal{R}_* \in (0, \infty). \quad (6)$$

In detachment mode, when the target particle is on the verge of detachment, the force balance in vertical direction satisfies the criterion $\mathbb{F}_L \geq \mathbb{F}_G$. Thus,

$$u_{z=z_\otimes}^2 \geq Q_D^2 = \frac{8\pi a^3 \Delta g}{3\mathcal{A}_f C_L} \forall\ \mathcal{R}_* \in (0, \infty). \quad (7)$$

From physical intuition [also evident from Eqs. (6) and (7)], we perceive that the inception of particle transport in detachment mode is greater than that in contact ($Q_D > Q_C$). The expressions of lever arms L_x and L_z are derived in Appendix B.

To determine the time-averaged critical boundary shear stress, we perform the averaging of Eqs. (6) and (7) over turbulence, yielding the time-averaged critical Shields numbers, Θ_{Cc} and Θ_{Dc}, in contact and detachment modes as

$$\Theta_{Cc}, \Theta_{Dc} = \frac{4\pi a^2}{3\mathcal{A}_f} \frac{u_{*c}^2}{(\bar{u}^2 + \sigma_u^2)_{z=z_\otimes}} \left[\frac{L_x}{C_D L_z + C_L L_x}, \frac{1}{C_L}\right], \quad (8)$$

where Θ is $u_*^2/(2a\Delta g)$ and σ_u is the streamwise turbulence intensity.

D. The laws of the wall and turbulence intensity

The flow regimes are distinguished by the shear Reynolds number $\mathcal{R}_*$. In a transitional flow regime ($3 < \mathcal{R}_* < 70$), the law of the wall proposed by Reichardt[45] used in this study is

$$\bar{u}(z) = \frac{u_*}{\kappa}\left\{\ln\left(1 + \kappa\frac{u_* z}{\nu}\right) - \left[1 - \exp\left(-\frac{1}{11.6}\frac{u_* z}{\nu}\right) - \frac{1}{11.6}\frac{u_* z}{\nu}\exp\left(-\frac{1}{3}\frac{u_* z}{\nu}\right)\right]\ln\left(\kappa\frac{u_* z_0}{\nu}\right)\right\}, \quad (9)$$

where κ is the von Kármán constant and z_0 is the zero-velocity level [Fig. 1(a)]. It is worth noting that Eq. (9) provides a reasonable estimation even for $\mathcal{R}_* < 3$ and $\mathcal{R}_* > 70$ over a certain range. Therefore, in this study, we apply Eq. (9) for the hydraulically smooth flow regime ($0.1 \leq \mathcal{R}_* \leq 3$) as well.

In a hydraulically rough flow regime ($\mathcal{R}_* \geq 70$), the law of the wall obeys the logarithmic law,

$$\bar{u}(z) = \frac{u_*}{\kappa}\ln\left(\frac{z}{z_0}\right). \quad (10)$$

Experimental observations revealed that the values of κ in a shear flow over mobile boundaries decrease from its universal value (= 0.41).[32,46] An average value of $\kappa = 0.385$ was reported by Best *et al.*[46] Then, van Rijn[19] argued that the logarithmic law over a boundary could be preserved fixing the virtual boundary level at $0.5r$ below the summits of the boundary particles (that is, $\xi = 0.25$) and considering the zero-velocity level $z_0 = 0.03\ k_s$. However, Dey *et al.*[32] reported that the ξ (=0.21) and the z_0 (=0.04 k_s) shift upward in case of weakly mobile boundaries. Therefore, in this study, we consider the values of $\kappa = 0.385$, $\xi = 0.21$, and $z_0 = 0.08r$.

The expression for the streamwise turbulence intensity σ_u is as follows:[47]

$$\sigma_u = 0.31(1 - \mathcal{V}_D)\frac{u_*^2 z}{\nu} + 2.3\mathcal{V}_D \exp\left(-\frac{z}{k_s}\right). \quad (11)$$

In Eq. (11), $\mathcal{V}_D$ is the van Driest damping function. It is given by $\mathcal{V}_D = 1 - \exp[u_* z(\mathcal{D}_f \nu)^{-1}]$, where $\mathcal{D}_f$ is the damping factor. The $\mathcal{D}_f$ can be considered as 10.[47]

III. STOCHASTIC ANALYSIS OF PARTICLE TRANSPORT

The stochastic analysis is carried out on the basis of the stochastic nature of instantaneous streamwise velocity in the immediate upstream vicinity of the target particle. The typical PDF $f_u(u|\mathbf{x}_p)$ of near-boundary instantaneous velocity $u(\mathbf{x}_p)$ in the immediate upstream vicinity of the particle is illustrated

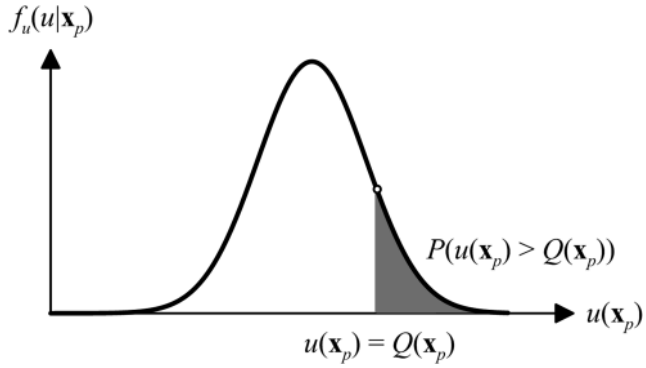

FIG. 3. Schematic of PDF $f_u(u|\mathbf{x}_p)$ of $u(\mathbf{x}_p)$.

in Fig. 3. The probability of u exceeding its critical value Q is represented by the shaded area in Fig. 3, and it is expressed as

$$P(u(\mathbf{x}_p) > Q(\mathbf{x}_p)) = \int_{Q(\mathbf{x}_p)}^{\infty} f_u(u|\mathbf{x}_p)\mathrm{d}u. \tag{12}$$

In Eq. (12), subscript p denotes the particle and the streamwise and vertical coordinates are given by $\mathbf{x}_p$ [$=(x_p, z_p)$]. Note that the critical value $Q(\mathbf{x}_p)$ is also a random variable due to variable boundary packing condition and pocket geometry. Thus, another PDF $f_Q[Q(\mathbf{x}_p)]$ of $Q(\mathbf{x}_p)$ is introduced in order to obtain the mean transport probability. It is then given by

$$\begin{aligned}\langle P\rangle &= \int_{-\infty}^{\infty} P(u(\mathbf{x}_p) > Q(\mathbf{x}_p))f_Q(Q(\mathbf{x}_p))\mathrm{d}u \\ &= \int_{-\infty}^{\infty}\left[\int_{Q(\mathbf{x}_p)}^{\infty} f_u(u|\mathbf{x}_p)\mathrm{d}u\right] f_Q(Q(\mathbf{x}_p))\mathrm{d}Q.\end{aligned} \tag{13}$$

A. PDFs of near-boundary instantaneous streamwise velocity and particle protrusion

Jiménez[40] reported that the velocity fluctuations in homogeneous turbulence are often close to a Gaussian distribution, although the high resolution data tend towards a non-Gaussian statistics. The non-Gaussian statistics result from the steepness of the energy spectrum and the properties of the energy containing eddies. In a turbulent wall shear layer flow, it was found that the Gram-Charlier (GC) PDF provides a satisfactory description of the near-boundary instantaneous velocity fluctuations.[48] The primary advantage of using the fourth-order GC PDF is that it involves the higher-order correlations to account for the important stochastic information related to the turbulent coherent structures. The fourth-order GC PDF of the near-boundary streamwise velocity fluctuations is given by

$$\begin{aligned}f_{\mathcal{U}}(\mathcal{U}_{z=z_\otimes}) = \Bigg\{&\frac{\exp(-0.5\mathcal{U}^2)}{(2\pi)^{1/2}}\left[1 + p_0(\mathcal{U}^3 - 3\mathcal{U})\right.\\ &\left. + p_1(\mathcal{U}^4 - 6\mathcal{U}^2 + 3)\right]\Bigg\}_{z=z_\otimes} \quad \forall\, \mathcal{U}_{z=z_\otimes} \in (-\infty,\ \infty),\end{aligned} \tag{14}$$

where U is u'/σ_u, p_0 is $S_u/6$, and p_1 is $(K_u - 3)/24$. The S_u and K_u are referred to as the skewness and kurtosis of u', respectively. Thus, S_u is $\overline{u'^3}/\sigma_u^3$ and K_u is $\overline{u'^4}/\sigma_u^4$. The PDF of the near-boundary instantaneous streamwise velocity is given by

$$f_u(u_{z=z_\otimes}) = \frac{1}{\sigma_u|_{z=z_\otimes}} f\left(\frac{u-\bar{u}}{\sigma_u}\right)_{z=z_\otimes} \quad \forall\, u_{z=z_\otimes} \in (-\infty,\ \infty). \tag{15}$$

Since the critical value $Q(\mathbf{x}_p)$ is a function of boundary packing and pocket geometry, the PDF of $Q(\mathbf{x}_p)$ can be replaced by considering the PDF of relative protrusion l^+ ($= l/2a$). Due to a complex geometry, an accurate description of the PDF of l^+ is a difficult proposition. However, the experiments evidenced that the l^+ can be considered as a uniformly distributed random variable.[49,50] Therefore, the PDF of l^+ is given by

$$f_{l^+}\{l^+ \in [0, l^+_{\max}]\} = 1/l^+_{\max}. \tag{16}$$

B. Higher-order moments of velocity fluctuations

Experimental observation of Antonia and Atkinson[51] showed that close to the boundary, the S_u is positive, whereas away from the boundary, it is negative. This suggests that in close proximity to the boundary, the large streamwise velocity fluctuations are primarily attributed to the arrival of high-speed fluid streaks from the region away from the boundary. In contrast, away from the boundary, the large streamwise velocity fluctuations are primarily attributed to the arrival of low-speed fluid streaks from the near-boundary flow region. On the other hand, the K_u decreases with an increase in vertical distance from the boundary becoming minimum in the close proximity of the boundary; and thereafter, it increases with the vertical distance.[52]

Interestingly, the K_u can be linked with the spectral slope α of the power spectrum $E(k) = k^\alpha$, where k is the wavenumber. Considering a one-dimensional case, Jiménez[40] showed that for a steep spectral slope ($\alpha < -1$), the $K_u(\alpha < -1) = 3(1 - 0.5S_2^{-2}S_4)$, where $S_n = \zeta(-0.5\alpha n)$ and ζ is the Riemann zeta function. It may be noted that the K_u ($\alpha \to -\infty$) = 1.5. On the other hand, for a mild spectral slope ($\alpha \geq -1$), the $K_u(\alpha \geq -1) = 3$. The main feature of $K_u(\alpha)$ is that the Gaussian distribution cannot be truly applicable in a homogeneous turbulent flow for variables whose spectral slopes are steeper than "−1" ($\alpha < -1$). Therefore, the velocity fluctuations, which are in general featured by the "−5/3" scaling law (spectral slope), depict a departure from the Gaussian distribution.

In this study, the S_u and K_u are considered as[35]

$$\begin{pmatrix} S_u \\ K_u \end{pmatrix} = \begin{pmatrix} p_{11} & p_{12} \\ p_{21} & p_{22} \end{pmatrix}\begin{pmatrix} 1 \\ \ln R_* \end{pmatrix}, \tag{17}$$

where $(p_{11},\ p_{12},\ p_{21},\ p_{22}) = (0,\ 0.102,\ 2.3,\ 0.136)\,\forall\,\mathcal{R}_* < 70$ and $(p_{11}, p_{12}, p_{21}, p_{22}) = (0.43, 0, 2.88, 0)\,\forall\,\mathcal{R}_* \geq 70$.

Figure 4 shows the fourth-order GC PDF of near-boundary streamwise velocity fluctuations for different shear Reynolds numbers $\mathcal{R}_* = 1$ (smooth), 12 (transitional), and 70 (rough), obtained from Eq. (14). The Gaussian PDF is also overlapped for the comparison. It is evident that with an increase in $\mathcal{R}_*$, the fourth-order GC PDFs become more peaked and skewed to the left (that is, positively skewed). It indicates that the arrival of high-speed fluid streaks in a hydraulically rough flow regime is at a much faster rate as compared to those in the hydraulically smooth and transitional flow regimes. Furthermore, the turbulence in a hydraulically rough flow regime is highly intermittent in the vicinity of the boundary as compared to that in the hydraulically smooth and transitional flow regimes. It is discernible that in the hydraulically smooth flow regime ($\mathcal{R}_* = 1$), the application of the Gaussian PDF overestimates the kurtosis of the fourth-order GC PDF, whereas in the hydraulically transitional flow regime ($\mathcal{R}_* = 12$), it overestimates the kurtosis of the fourth-order GC PDF and underestimates the

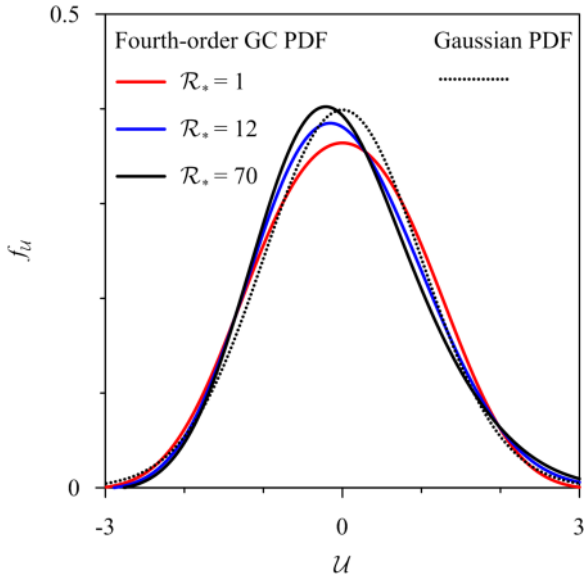

FIG. 4. Typical PDF $f_{\mathcal{U}}$ of near-boundary streamwise velocity fluctuations $\mathcal{U}$.

skewness of the fourth-order GC PDF. On the other hand, in the hydraulically rough flow regime ($\mathcal{R}_* = 70$), the Gaussian PDF underestimates the skewness of the fourth-order GC PDF. Another drawback of employing the Gaussian PDF in characterizing the instantaneous velocity (or the velocity fluctuations) is that the Gaussian PDF is invariant of $\mathcal{R}_*$, as evident from Fig. 4. Thus, it is unable to capture the differences in transport processes in different flow regimes. Moreover, the Gaussian PDF does not account for the higher order moments, which are essential for understanding the dynamics of near-boundary turbulence structures.

C. Probabilities of particle transport

The probability P_C of particle transport in contact mode is expressed as

$$\begin{aligned} P_C &= P[u^2_{z=z_\otimes} \in (Q_C^2, Q_D^2)] \\ &= P[u_{z=z_\otimes} \in (-Q_D, -Q_C)] + P[u_{z=z_\otimes} \in (Q_C, Q_D)] \\ &= \left[\int_{-Q_D}^{-Q_C} f_u(u)\mathrm{d}u + \int_{Q_C}^{Q_D} f_u(u)\mathrm{d}u \right]_{z=z_\otimes} \\ &= \left[\int_{-\frac{Q_D+\bar{u}}{\sigma_u}}^{-\frac{Q_C+\bar{u}}{\sigma_u}} f_{\mathcal{U}}(\mathcal{U})\mathrm{d}\mathcal{U} + \int_{\frac{Q_C-\bar{u}}{\sigma_u}}^{\frac{Q_D-\bar{u}}{\sigma_u}} f_{\mathcal{U}}(\mathcal{U})\mathrm{d}\mathcal{U} \right]_{z=z_\otimes} = \sum_{j=1}^{4} (-1)^j H(a_j). \end{aligned} \tag{18}$$

In Eq. (18), the $H(a_j)$ is given by

$$H(a_j) = \frac{1}{2}\mathrm{erf}\left(\frac{a_j}{2^{1/2}}\right) - \frac{1}{(2\pi)^{1/2}} \times \frac{\exp(-0.5a_j^2)[4(a_j^2-1)S_u + a_j(a_j^2-3)(K_u-3)]}{24}, \tag{19}$$

and a_j, after using Eqs. (6) and (7), can be expressed as

$$a_j = -\frac{1}{\lambda}\left\{ \mathrm{sgn}(m_1)\left(\frac{8\pi\Delta g a^3}{3\mathcal{A}_f \bar{u}^2_{z=z_\otimes}}\right)^{1/2} \times \left[m_2 \frac{1}{C_L} + m_3 \frac{L_x}{C_D L_z + C_L L_x} \right]^{1/2} + 1 \right\}, \tag{20}$$

where λ is $(\sigma_u/\bar{u})_{z=z_\otimes}$, $m_1(j=1,2) > 0$, $m_1(j=3,4) < 0$, $(m_2, m_3) = (1, 0)$ for $j = 1, 4$, and $(m_2, m_3) = (0, 1)$ for $j = 2, 3$.

On the other hand, the probability P_D of particle transport in detachment mode is expressed as

$$\begin{aligned} P_D &= P[u^2_{z=z_\otimes} \in (Q_D^2, \infty)] = 1 - P[u_{z=z_\otimes} \in (-Q_D, Q_D)] \\ &= 1 - \left[\int_{-Q_D}^{Q_D} f_u(u)\mathrm{d}u \right]_{z=z_\otimes} \\ &= 1 - \left[\int_{-\frac{Q_D+\bar{u}}{\sigma_u}}^{\frac{Q_D-\bar{u}}{\sigma_u}} f_{\mathcal{U}}(\mathcal{U})\mathrm{d}\mathcal{U} \right]_{z=z_\otimes} = 1 + H(a_1) - H(a_4). \end{aligned} \tag{21}$$

The mean transport probabilities, $\langle P_C \rangle$ and $\langle P_D \rangle$, in contact and detachment modes are the mean values of Eqs. (18) and (21), respectively. They are expressed as

$$\langle P_C, P_D \rangle = \int_0^{l^+_{\max}} (P_C, P_D) f_{l^+}(l^+)\mathrm{d}l^+. \tag{22}$$

IV. RESULTS AND DISCUSSION

To prepare the graphical illustrations, characteristic values of ρ_p, ρ_f, and ν are considered as 2.65×10^3 kg m^{-3}, 10^3 kg m^{-3}, and 10^{-6} m^2 s^{-1}, respectively.

A. Mean transport probabilities in contact and detachment modes

To explore the particle transport phenomenon, we are interested to know the transport probabilities for a given relative particle size $\mathcal{N}$. It provides a continuum description of the transport probabilities of particles rather than limiting the transport phenomenon from a discrete viewpoint. The mean transport probabilities, $\langle P_C \rangle$ and $\langle P_D \rangle$, in contact and detachment modes, therefore, represent a comprehensive picture of the stochastic characteristics of the particles over the full range of protrusion or packing density. The $\langle P_C \rangle$ and $\langle P_D \rangle$ are computed from Eq. (22).

The variations of mean transport probabilities, $\langle P_C \rangle$ and $\langle P_D \rangle$, in contact and detachment modes with Shields number Θ for different relative particle sizes $\mathcal{N} = 0.25$, 0.5, 1, and 1.5 and shear Reynolds numbers $\mathcal{R}_*$ (= 1, 12, and 100) are furnished in Figs. 5(a)–5(c). For all the values of $\mathcal{R}_*$, the $\langle P_C \rangle$ decreases with an increase in $\mathcal{N}$ up to the occurrence of a peak of the $\langle P_C \rangle(\Theta)$ for $\mathcal{N} = 0.25$, and thereafter, for a larger Θ, the $\langle P_C \rangle$ increases with an increase in $\mathcal{N}$. On the other hand, for a given Θ, the $\langle P_D \rangle$ decreases with an increase in $\mathcal{N}$. For a given $\mathcal{N}$, the peak of the $\langle P_C \rangle(\Theta)$ occurs early in the hydraulically smooth flow regime ($\mathcal{R}_* = 1$) than those in the hydraulically

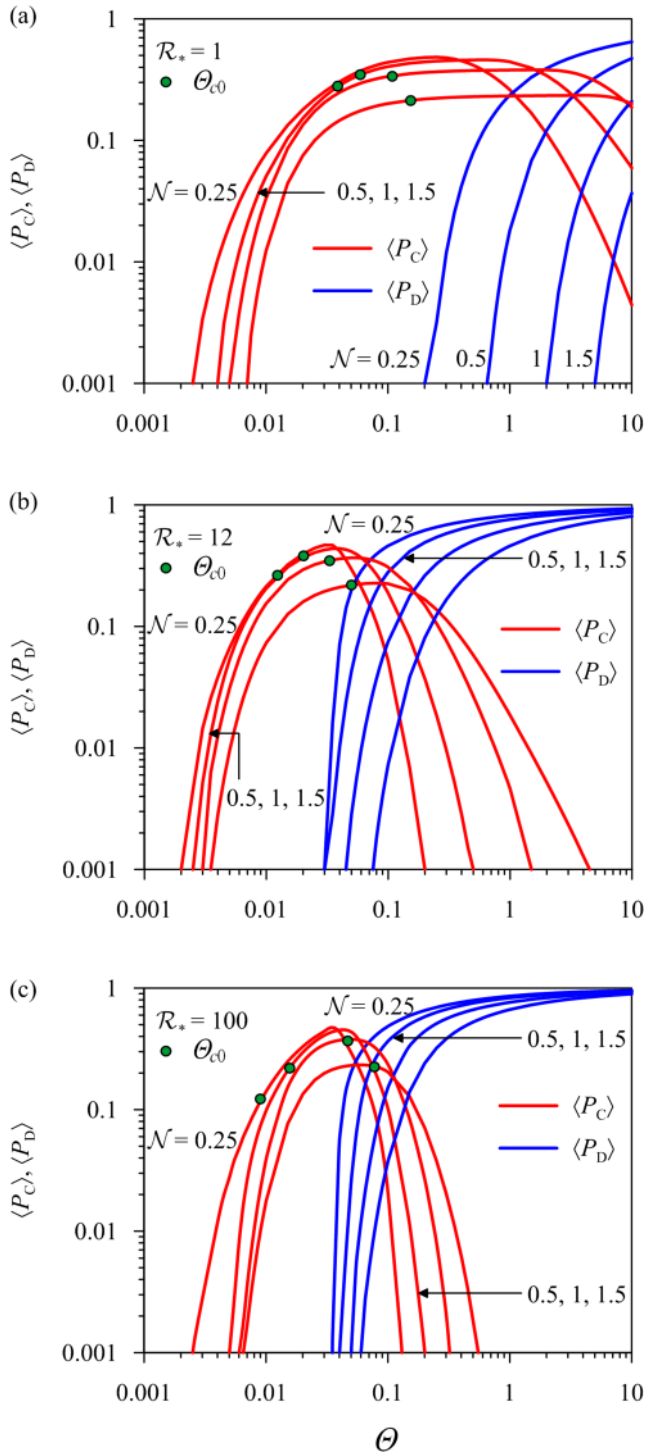

FIG. 5. Variations of mean transport probabilities, $\langle P_C \rangle$ and $\langle P_D \rangle$, in contact and detachment modes with Shields number Θ for different relative particle sizes $\mathcal{N}$ (= 0.25, 0.5, 1, and 1.5) and shear Reynolds numbers (a) $\mathcal{R}_* = 1$, (b) $\mathcal{R}_* = 12$, (c) $\mathcal{R}_* = 100$. The points of averaged critical Shields number Θ_{c0} are marked on $\langle P_C \rangle(\Theta)$ curves.

transitional ($\mathcal{R}_* = 12$) and rough ($\mathcal{R}_* = 100$) flow regimes. Further, for a given $\mathcal{N}$, the separation between the rising and the recession limbs of the $\langle P_C \rangle(\Theta)$ curve is narrowed down with an increase in $\mathcal{R}_*$. The separation between the $\langle P_D \rangle(\Theta)$ curves for different $\mathcal{N}$ values is also narrowed down with an increase in $\mathcal{R}_*$.

To be more specific, it is further evident that for all the values of $\mathcal{R}_*$, the $\langle P_C \rangle$ increases with an increase in Θ attaining a peak and then decreases. On the other hand, the $\langle P_D \rangle$ increases monotonically with an increase in Θ. The averaged critical Shields numbers Θ_{c0} for different $\mathcal{N}$ and $\mathcal{R}_*$, obtained from the $\Theta_{c0}(\mathcal{R}_*)$ curves,[53] are also marked on the $\langle P_C \rangle(\Theta)$ curves in Figs. 5(a)–5(c). Interestingly, in the hydraulically transitional ($\mathcal{R}_* = 12$) and rough ($\mathcal{R}_* = 100$) flow regimes, the $\langle P_D \rangle(\Theta)$ curves for $\mathcal{N} \geq 1$ almost attain their peaks at $\Theta \approx \Theta_{c0}$, and the $\langle P_D \rangle(\Theta)$ curves initiate from that point ($\Theta = \Theta_{c0}$). Figs. 5(a)–5(c) show that in the hydraulically transitional ($\mathcal{R}_* = 12$) and rough ($\mathcal{R}_* = 100$) flow regimes, the dominant mode of transport for a smaller Θ (approximately $\Theta < 0.1$) is contact, while for a larger Θ (approximately $\Theta > 0.2$), the particles primarily transport as a detachment mode. These results are in conformity with the argument of Hu and Guo.[54] Based on the experimental observations of Hu and Hui,[55] Hu and Guo[54] reported that the contact mode is dominant for $\Theta < 0.1$, while the detachment mode is prevalent for $\Theta > 0.2$ for $\mathcal{N} = 1$. A qualitative description of the transport probabilities in contact and detachment modes in a hydraulically transitional flow regime was given using the visual observation of bedload transport of uniform fine gravels ($\mathcal{N} = 1$), as was done by Drake *et al.*[56] They found that for $\Theta < 0.12$, the dominant mode of transport is contact, while for $\Theta > 0.18$, the dominant mode of transport is detachment. Reverting to this study, the $\langle P_C \rangle(\Theta)$ and $\langle P_D \rangle(\Theta)$ curves in the hydraulically transitional flow regime ($\mathcal{R}_* = 12$) completely corroborate with the qualitative observation of Drake *et al.*[56]

The variations of mean transport probabilities, $\langle P_C \rangle$ and $\langle P_D \rangle$, in contact and detachment modes with Shields number Θ for a relative particle size $\mathcal{N} = 1$ and a shear Reynolds number $\mathcal{R}_* = 100$ (hydraulically rough flow regime) are further depicted in Fig. 6. The $\langle P_D \rangle(\Theta)$ curve obtained by Wu and Yang[35] is also shown for the comparison. It may be noted that Wu and Yang[35] did not calculate the $\langle P_C \rangle(\Theta)$ curve. The experimental data of $\langle P_C \rangle(\Theta)$[55] and $\langle P_D \rangle(\Theta)$[55,57–60] are also plotted for the validation of the model results. In particular, the $\langle P_C \rangle(\Theta)$ curve shown in Fig. 6 underestimates the experimental data of $\langle P_C \rangle(\Theta)$. The reason is attributed to the fact

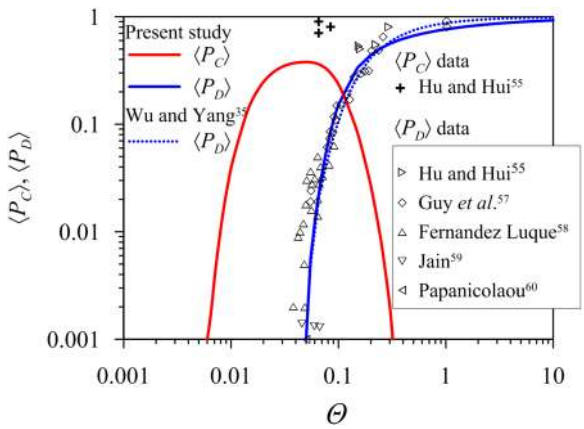

FIG. 6. Variations of mean transport probabilities, $\langle P_C \rangle$ and $\langle P_D \rangle$, in contact and detachment modes with Shields number Θ for a relative particle size $\mathcal{N} = 1$ and a shear Reynolds number $\mathcal{R}_* = 100$.

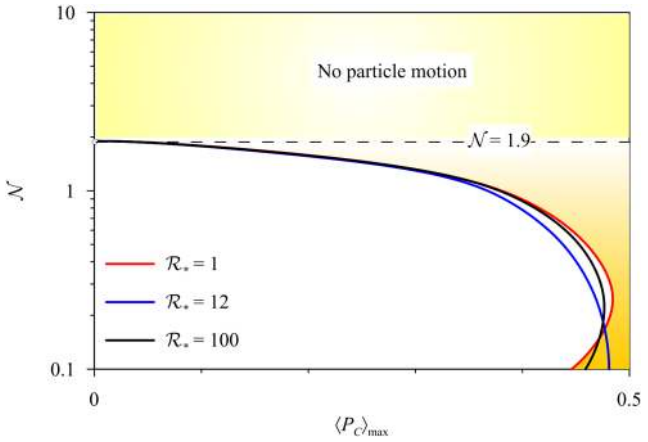

FIG. 7. Variation of maximum mean transport probability $\langle P_C \rangle_{\max}$ in contact mode with relative particle size $\mathcal{N}$ for different shear Reynolds numbers $\mathcal{R}_*$ (= 1, 12, and 100).

that the theoretical $\langle P_C \rangle(\Theta)$ curve signifies the mean probability curve being averaged over the entire range of particle protrusion. However, the experimental data of $\langle P_C \rangle(\Theta)$ can be considered for the surface particles which are more protruded than the remaining particles whose transport in contact mode is less probable. The $\langle P_D \rangle(\Theta)$ curve, in general, corresponds well with the experimental data for $C_L = 0.3$. Specifically, the experimental data of Guy *et al.*[57] involved a dunal flow regime. Moreover, for a larger Θ, an increasing number of transported boundary particles can cause a flow retardation in the close proximity of the boundary. As a consequence, such flow retardation can affect the resulting PDF.

The maximum mean transport probability $\langle P_C \rangle_{\max}$ in contact mode as a function of relative particle size $\mathcal{N}$ for different shear Reynolds numbers $\mathcal{R}_*$ (= 1, 12, and 100) is illustrated in Fig. 7. In the hydraulically smooth ($\mathcal{R}_* = 1$) and rough ($\mathcal{R}_* = 100$) flow regimes, both the $\langle P_C \rangle_{\max}$ slowly increase with an increase in $\mathcal{N}$ and after attaining their individual peak values, they reduce with a further increase in $\mathcal{N}$. However, for the hydraulically transitional flow regime ($\mathcal{R}_* = 12$), the $\langle P_C \rangle_{\max}$ decreases with an increase in $\mathcal{N}$. Remarkably, for $\mathcal{N} \geq 1$, all the $\mathcal{N}(\langle P_C \rangle_{\max})$ curves merge together, suggesting that the $\langle P_C \rangle_{\max}$ is virtually independent of $\mathcal{R}_*$ for $\mathcal{N} \geq 1$. Another important aspect of Fig. 7 is that for $\mathcal{N} \geq 1.9$, the $\langle P_C \rangle_{\max}$ for all the $\mathcal{R}_*$ becomes absolutely zero, indicating that for $\mathcal{N} \geq 1.9$, the mean transport probability in contact mode essentially vanishes. This phenomenon is practically feasible because for a larger $\mathcal{N}(\mathcal{N} \geq 1.9)$, the probability of a particle to be transported in a contact mode becomes vanishingly small since the target particle receives weak hydrodynamic forces due to hiding of the particle within the pocket of the boundary particles for all possible protrusions. Therefore, the critical value of $\mathcal{N}$, for which the mean probability of the particle transport in contact mode vanishes, is 1.9. Since every point on the $\mathcal{N}(\langle P_C \rangle_{\max})$ curves represents the maximum mean probability of particle transport in contact mode, the space on the right side of the $\mathcal{N}(\langle P_C \rangle_{\max})$ curves therefore represents no particle transport in contact mode.

B. Mean transport probabilities in contact and detachment modes at an inception of particle transport

Here, we are interested to investigate the characteristics of mean transport probabilities at an inception in contact and detachment modes. The variations of mean transport probabilities at an inception, $\langle P_C \rangle_c$ and $\langle P_D \rangle_c$, in contact and detachment modes with critical shear Reynolds number $\mathcal{R}_{*c}$ for different relative particle sizes $\mathcal{N}$ = 0.25, 0.5, 1, and 1.5 are demonstrated in Fig. 8. For a given $\mathcal{N}$ and $\mathcal{R}_{*c}$, the Θ_{Cc} and Θ_{Dc} corresponding to the mean l^+ are first obtained from Eq. (8). Then, the $\langle P_C \rangle_c(\mathcal{R}_{*c})$ and $\langle P_D \rangle_c(\mathcal{R}_{*c})$ are obtained from the proposed $\langle P_C \rangle(\Theta)$ and $\langle P_D \rangle(\Theta)$ relationships as developed in Eq. (22). It is evident that the $\langle P_C \rangle_c(\mathcal{R}_{*c})$ and $\langle P_D \rangle_c(\mathcal{R}_{*c})$ marginally increase with an increase in $\mathcal{R}_{*c}$. However, for a given $\mathcal{R}_{*c}$, the $\langle P_C \rangle_c(\mathcal{R}_{*c})$ and $\langle P_D \rangle_c(\mathcal{R}_{*c})$ decrease with an increase in $\mathcal{N}$. Overall, the variations of $\langle P_C \rangle_c(\mathcal{R}_{*c})$ with $\mathcal{N}$ are more prominent than that of $\langle P_D \rangle_c(\mathcal{R}_{*c})$ with $\mathcal{N}$. Importantly, the $\langle P_C \rangle_c(\mathcal{R}_{*c})$ and $\langle P_D \rangle_c(\mathcal{R}_{*c})$ become invariant of $\mathcal{R}_{*c}$ for $\mathcal{R}_{*c} > 100$ and $\mathcal{R}_{*c} > 70$, respectively.

The variations of mean transport probabilities at an inception, $\langle P_C \rangle_c$ and $\langle P_D \rangle_c$, in contact and detachment modes with critical Shields number Θ_c for different relative particle sizes $\mathcal{N}$ = 0.25, 0.5, 1, and 1.5 are illustrated in Fig. 9. Figure 9 reveals that for a given Θ_c, the $\langle P_C \rangle_c(\Theta_c)$ and $\langle P_D \rangle_c(\Theta_c)$ decrease with an increase in $\mathcal{N}$. However, the $\langle P_C \rangle_c(\Theta_c)$ and $\langle P_D \rangle_c(\Theta_c)$ curves comprise of three segments separated by two small circles. These segments represent the domains of different flow regimes (smooth, transitional, and rough). The evolution of $\langle P_C \rangle_c(\Theta_c)$ and $\langle P_D \rangle_c(\Theta_c)$ curves is shown by the curved arrow tips. In a hydraulically smooth flow regime, the $\langle P_C \rangle_c$, originating from the right tail of the $\langle P_C \rangle_c(\Theta_c)$ curve, increases with a decrease in Θ_c. On the other hand, in a hydraulically transitional flow regime, the $\langle P_C \rangle_c$ increases with a decrease in Θ_c attaining a critical value (minimum value of Θ_c) and then increases [the $\langle P_C \rangle_c(\Theta_c)$ curve takes a sharp turn towards right] with an increase in Θ_c. However, in a hydraulically rough flow regime, the $\langle P_C \rangle_c$ slowly increases with Θ_c becoming a constant. Importantly, for a given $\mathcal{N}$ and a specific value of Θ_c, two values of $\langle P_C \rangle_c$ are obtained. These two values of $\langle P_C \rangle_c(\Theta_c)$ curve correspond to the same or two different flow regimes. For instance, for $\mathcal{N}$ = 0.25, 0.5, and 1, two values of $\langle P_C \rangle_c$

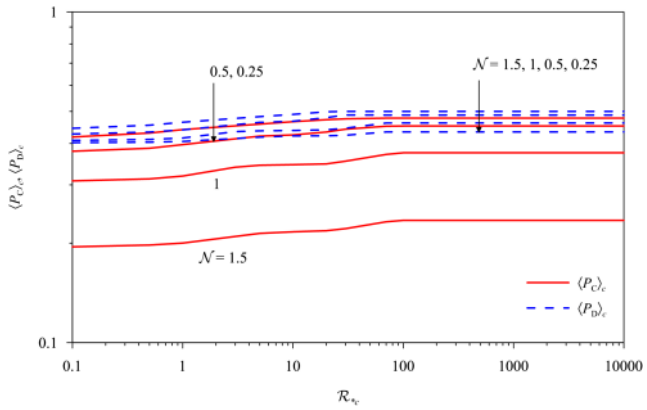

FIG. 8. Variations of mean transport probabilities at an inception, $\langle P_C \rangle_c$ and $\langle P_D \rangle_c$, in contact and detachment modes with critical shear Reynolds number $\mathcal{R}_{*c}$ for different relative particle sizes $\mathcal{N}$ (= 0.25, 0.5, 1, and 1.5).

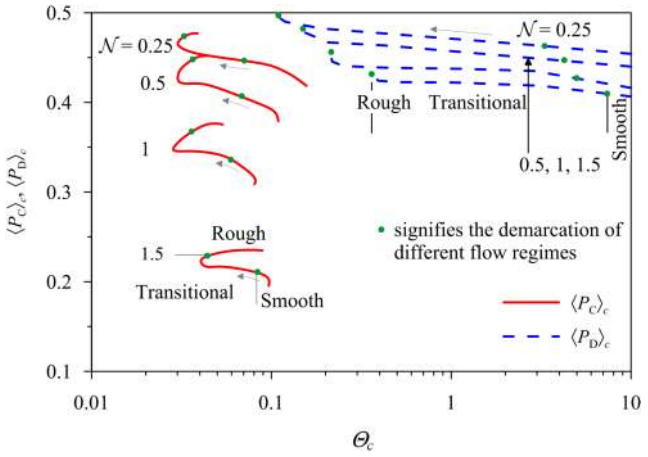

FIG. 9. Variations of mean transport probabilities at an inception, $\langle P_C\rangle_c$ and $\langle P_D\rangle_c$, in contact and detachment modes with critical Shields number Θ_c for different relative particle sizes $\mathcal{N}$ (= 0.25, 0.5, 1, and 1.5).

correspond to the hydraulically transitional and transitional-rough flow regimes, while for $\mathcal{N}$ = 1.5, two values of $\langle P_C\rangle_c$ correspond to the hydraulically transitional, transitional-rough, and smooth-rough flow regimes. Further, the $\langle P_D\rangle_c(\Theta_c)$ increases with a decrease in Θ_c becoming a constant at the extremity of the hydraulically transitional flow regime. Importantly, this extremity represents the hydraulically rough flow regime, as in a hydraulically rough flow regime ($\mathcal{R}_{*c} \geq 70$), the $\langle P_D\rangle_c(\mathcal{R}_{*c})$ is invariant of $\mathcal{R}_{*c}$ (Fig. 8).

Therefore, this study is capable to capture the essential stochastic processes of loose boundary particle transport elucidating the underlying physics. In this regard, it is important to note that Ali and Dey[30] deterministically analyzed the inception of particle transport based on a static configuration of compact boundary particles. Moreover, a preliminary stochastic analysis by Dey and Ali[36] assumed an idealized configuration of compact boundary particles. They characterized the near-boundary instantaneous streamwise velocity by the log-normal probability density function. By contrast, the core content of this study focuses on a new realistic stochastic notion of boundary particle transport by treating a more generalized configuration of loose (non-compact) boundary particles and by applying a more suitable fourth-order Gram-Charlier probability density function of the near-boundary instantaneous streamwise velocity. Further, the most important features that are the relationships of the mean transport probabilities with the Shields number for different relative particle sizes and shear Reynolds numbers were not studied by Dey and Ali.[36]

Finally, this study can be effectively applied in various engineering disciplines including fluvial morphodynamics. For example, for a given flow condition, the sediment particle transport in a gravel-bed stream is generally accompanied by a partial transport condition, where active particles being exposed at the surface are transported sporadically. In contrast, the partially exposed particles remain immobile for the same flow condition. However, under a full-transport condition, almost all the sediment particles at the surface are transported into the bedload layer. This study effectively addresses such features to model the transport phenomenon of mixed-size sediment particles. The mean transport probabilities, in contact and detachment modes, for a given relative size of particles can be helpful in assessing the entrainment risk, flushing flow carrying excess amount of sediment particles, proper design to channel networks, and protective measures against erosion.

V. CONCLUSION

We explore the turbulent wall shear flow driven transport of near-boundary particles having variable protrusions due to variable boundary packing densities considering the micromechanics of the cohesionless boundary particles in a 3-D organization and using the laws of the wall for hydraulically smooth, transitional, and rough flows. The criteria for particle transport in contact and detachment modes are obtained by applying the equilibria of the force moments and the forces, respectively. The mean transport probabilities in contact and detachment modes are obtained as a function of Shields number for different relative particle sizes and shear Reynolds numbers. For a given relative particle size, the mean transport probability in contact mode increases with an increase in Shields number to attain its peak value and then decreases. On the other hand, the mean transport probability in detachment mode increases monotonically with an increase in Shields number. One of the interesting features is that for the hydraulically transitional and rough flow regimes, the transport probabilities in contact mode for a given relative particle size of greater than or equal to unity attain their peak values corresponding to the averaged critical Shields numbers, where the transport probabilities in detachment mode have their initiation. The curves of maximum mean transport probability in contact mode as a function of relative particle size for different shear Reynolds numbers are furnished. The influence of shear Reynolds number on these curves is prominent only for a relative particle size being less than unity. For a relative particle size of 1.9 and above, the maximum mean transport probability in contact mode for different shear Reynolds numbers vanishes.

At an inception of particle transport, the variation of mean transport probabilities in contact and detachment modes with shear Reynolds number for different relative particle sizes reveals that the mean transport probabilities marginally increase with an increase in shear Reynolds number. However, for a given shear Reynolds number, the mean transport probabilities in these modes decrease with an increase in relative particle size. For a given relative particle size, the mean transport probability at an inception in contact mode increases with a decrease in critical Shields number, attaining a minimum value of critical Shields number and then increases with an increase in critical Shields number. However, the mean transport probability at an inception in detachment mode increases with a decrease in critical Shields number.

ACKNOWLEDGMENTS

The authors are thankful to Thanos Papanicolaou, Fu-Chun Wu, and Yi-Ju Chou for reviewing and providing the suggestions during the preparation of the manuscript.

APPENDIX A: RELATIONSHIP OF MEAN PIVOTING ANGLE WITH PARTICLE SIZES AND PROTRUSION

Referring to Fig. 1(b), let δ be the distance of the bottommost point of the target particle from $z = 0$. Thus, we can write $\delta = r(2\xi - 1) - a + d_{CJ}$ [Fig. 1(c)], where d_{CJ} denotes the distance between points C and J. If ϕ_1 is the angle making the line connecting the center of the target particle to one of the points of contact with the vertical line passing through the center of the target particle, then we can write $d_{CJ} = (a + r)\cos\phi_1$. Therefore, we get $\delta = 2\xi r - (a + r)(1 - \cos\phi_1)$. Further with respect to Fig. 1(b), we obtain $\delta = 2\xi r + l - 2a$. Equating these relationships of δ yields

$$\phi_1 = \cos^{-1}\left(\frac{r - a + l}{a + r}\right). \tag{A1}$$

In a contact mode, when the target particle rolls in the direction JC_2, the pivoting angle is ϕ_1 [Fig. 1(c)]. On the other hand, when the target particle rolls in the direction JP, the pivoting angle is ϕ_2 [Fig. 1(c)]. When the target particle is fully protruded, the l attains its peak value $l_{\max}$ and the corresponding pivoting angle ϕ_1 attains its minimum value. For such a situation, we get $d_{C_2J} = 2r/3^{1/2}$. Therefore, the $\phi_{1\min}$ is given by

$$\phi_{1\,\min} = \cos^{-1}\left(\frac{d_{CJ}}{d_{CC_2}}\right) = \cos^{-1}\left[\frac{(6a + 12r - 4r^2)^{1/2}}{2\sqrt{3}(a + r)}\right]. \tag{A2}$$

Equating (A1) and (A2) yields

$$l_{\max} = a - r + \frac{(6a + 12r - 4r^2)^{1/2}}{2\sqrt{3}}. \tag{A3}$$

Let the most likely path followed by the target particle during the contact mode be in the direction JQ, where $JQ \in [JP, JC_2]$. For such a situation, the mean pivoting angle $\angle QCJ$ is $\phi_m \in [\phi_2, \phi_1]$. Considering an angle $\angle PJQ = \theta$, the mean value of d_{JQ} is obtained as

$$d_{JQ} = \frac{3}{\pi}\int_0^{\pi/3} d_{JQ}\mathrm{d}\theta = \frac{3}{2\pi}\ln(2 + \sqrt{3})[(2r + l)(2a - l)]^{1/2}. \tag{A4}$$

From the geometry, we have the ratio $d_{IK}/d_{JQ} = a/(a + r)$ and the $d_{CI} = a\cos\phi_1$. Therefore, the mean pivoting angle ϕ_m is

$$\phi_m = \tan^{-1}\frac{d_{IK}}{d_{CI}} = \tan^{-1}\left[\frac{1}{\cos\phi_1(a + r)}d_{JQ}\right]. \tag{A5}$$

Substituting (A1) and (A4) into (A5) yields

$$\phi_m = \tan^{-1}\left\{\frac{3\ln(2 + \sqrt{3})[(2a - l)(2r + l)]^{1/2}}{2\pi(r + l - a)}\right\}. \tag{A6}$$

APPENDIX B: DETERMINATION OF MOMENT ARMS

Depending on the flow direction with respect to the orientation of the boundary particles, the moments of the forces $\mathbb{F}_D$, $\mathbb{F}_L$, and $\mathbb{F}_G$ are taken about the point G_2 or the line G_2G_3 [Fig. 1(c)]. The horizontal lever arms for various orientations vary within two bounds as d_{G_2I} and d_{HI}. Thus, for an arbitrary streamwise orientation of the boundary particles, the L_x must satisfy $L_x \in [d_{G_2I}, d_{HI}]$. Hence, the mean value of L_x is $L_x = d_{IK}$ [Fig. 1(c)]. From the geometry, the L_x is given by

$$L_x = \frac{3a\,\ln(2 + \sqrt{3})[(2r + l)(2a - l)]^{1/2}}{2\pi(a + r)}. \tag{B1}$$

Then, the vertical lever arm is expressed as $L_z = d_{C_0I} = z_\otimes - \delta - a(1 - \cos\phi_1)$ [Fig. 1(c)]. Using the expression of δ $(= 2\xi r + l - 2a)$ and (A1), the L_z is given by

$$L_z = z_\otimes - 2\xi r + \frac{(2a - l)r}{a + r}. \tag{B2}$$

[1] R. A. Bagnold, *The Physics of Blown Sand and Desert Dunes* (Chapman and Hall, London, 1941).
[2] H. A. Einstein, "The bed-load function for sediment transportation in open channel flows," *Technical Bulletin* (United States Department of Agriculture, Soil Conservation Service, Washington DC, USA, 1950), 1026.
[3] K. Nishimura and J. C. R. Hunt, "Saltation and incipient suspension above a flat particle bed below a turbulent boundary layer," J. Fluid Mech. **417**, 77–102 (2000).
[4] Y.-H. Zhou, X. Guo, and X. J. Zheng, "Experimental measurement of wind-sand flux and sand transport for naturally mixed sands," Phys. Rev. E **66**, 021305 (2002).
[5] A. Gyr and W. Kinzelbach, "Bed forms in turbulent channel flow," Appl. Mech. Rev. **57**, 77–93 (2004).
[6] F. Charru, B. Andreotti, and P. Claudin, "Sand ripples and dunes," Annu. Rev. Fluid Mech. **45**, 469–493 (2013).
[7] S. Dey, *Fluvial Hydrodynamics: Hydrodynamic and Sediment Transport Phenomena* (Springer-Verlag, Berlin, Germany, 2014).
[8] J. Capecelatro and O. Desjardins, "Eulerian-Lagrangian modeling of turbulent liquid–solid slurries in horizontal pipes," Int. J. Multiphase Flow **55**, 64–79 (2013).
[9] B. Arcen, A. Tanière, and M. Khalij, "Heat transfer in a turbulent particle-laden channel flow," Int. J. Heat Mass Transfer **55**, 6519–6529 (2012).
[10] B. Lessani and M. H. Nakhaei, "Large-eddy simulation of particle-laden turbulent flow with heat transfer," Int. J. Heat Mass Transfer **67**, 974–983 (2013).
[11] J. R. Finn and M. Li, "Regimes of sediment-turbulence interaction and guidelines for simulating the multiphase bottom boundary layer," Int. J. Multiphase Flow **85**, 278–283 (2016).
[12] C. M. White, "The equilibrium of grains on the bed of a stream," Proc. R. Soc. London, Ser. A **174**, 322–338 (1940).
[13] A. D. Heathershaw and P. D. Thorne, "Sea-bed noises reveal role of turbulent bursting phenomenon in sediment transport by tidal currents," Nature **316**, 339–342 (1985).
[14] C. Villaret and A. G. Davies, "Modeling sediment-turbulent flow interactions," Appl. Mech. Rev. **48**, 601–609 (1995).
[15] C. Ji, A. Munjiza, E. Avital, J. Ma, and J. J. R. Williams, "Direct numerical simulation of sediment entrainment in turbulent channel flow," Phys. Fluids **25**, 056601 (2013).
[16] C. Ji, A. Munjiza, E. Avital, D. Xu, and J. Williams, "Saltation of particles in turbulent channel flow," Phys. Rev. E **89**, 052202 (2014).
[17] P. Nielsen, "Suspended sediment concentration profiles," Appl. Mech. Rev. **48**, 564–569 (1995).
[18] S. Z. Ali and S. Dey, "Mechanics of advection of suspended particles in turbulent flow," Proc. R. Soc. London, Ser. A **472**, 20160749 (2016).
[19] L. C. van Rijn, "Sediment transport. I: Bed load transport," J. Hydraul. Eng. **110**, 1431–1456 (1984).
[20] J. S. Bridge and S. J. Bennett, "A model for the entrainment and transport of sediment grains of mixed sizes, shapes, and densities," Water Resour. Res. **28**, 337–363 (1992).
[21] M. G. Kleinhans and L. C. van Rijn, "Stochastic prediction of sediment transport in sand-gravel bed rivers," J. Hydraul. Eng. **128**, 412–425 (2002).
[22] C. Ancey, T. Böhm, M. Jodeau, and P. Frey, "Statistical description of sediment transport experiments," Phys. Rev. E **74**, 011302 (2006).
[23] F. Osanloo, M. R. Kolahchi, S. McNamara, and H. J. Herrmann, "Sediment transport in the saltation regime," Phys. Rev. E **78**, 011301 (2008).

[24]C. Ancey, "Stochastic modeling in sediment dynamics: Exner equation for planar bed incipient bed load transport conditions," J. Geophys. Res. **115**, F00A11, doi:10.1029/2009jf001260 (2010).
[25]J. R. Agudo and A. Wierschem, "Incipient motion of a single particle on regular substrates in laminar shear flow," Phys. Fluids **24**, 093302 (2012).
[26]M. Tregnaghi, A. Bottacin-Busolin, A. Marion, and S. Tait, "Stochastic determination of entrainment risk in uniformly sized sediment beds at low transport stages: 1. Theory," J. Geophys. Res. **117**, F04004, doi:10.1029/2011jf002134 (2012).
[27]A. H. Clark, M. D. Shattuck, N. T. Ouellette, and C. S. O'Hern, "Onset and cessation of motion in hydrodynamically sheared granular beds," Phys. Rev. E **92**, 042202 (2015).
[28]M. Houssais, C. P. Ortiz, D. J. Durian, and D. J. Jerolmack, "Onset of sediment transport is a continuous transition driven by fluid shear and granular creep," Nat. Commun. **6**, 6527 (2015).
[29]A. F. Shields, "Application of similarity principles and turbulence research to bed-load movement," in *Mitteilungen der Preussischen Versuchsanstalt für Wasserbau und Schiffbau* (Hydrodynamics Laboratory, Germany, Berlin, 1936), Vol. 26, pp. 5–24, http://resolver.caltech.edu/CaltechKHR:HydroLabpub167.
[30]S. Z. Ali and S. Dey, "Hydrodynamics of sediment threshold," Phys. Fluids **28**, 075103 (2016).
[31]S. J. Kline, W. C. Reynolds, F. A. Schraub, and P. W. Runstadler, "The structure of turbulent boundary layers," J. Fluid Mech. **30**, 741–773 (1967).
[32]S. Dey, R. Das, R. Gaudio, and S. K. Bose, "Turbulence in mobile-bed streams," Acta Geophys. **60**, 1547–1588 (2012).
[33]Y. Niño and M. H. Garcia, "Experiments on particle-turbulence interactions in the near-wall region of an open channel flow: Implications for sediment transport," J. Fluid Mech. **326**, 285–319 (1996).
[34]F.-C. Wu and Y.-J. Chou, "Rolling and lifting probabilities for sediment entrainment," J. Hydraul. Eng. **133**, 329–334 (2003).
[35]F.-C. Wu and K.-H. Yang, "Entrainment probabilities of mixed-size sediment incorporating near-bed coherent flow structures," J. Hydraul. Eng. **130**, 1187–1197 (2004).
[36]S. Dey and S. Z. Ali, "Hydrodynamics of sediment transport: Grain scale to continuum scale," in *Proceedings of Eighth International Conference on Scour and Erosion (ICSE-2016)* (CRC Press, 2016).
[37]B. Vowinckel, T. Kempe, and J. Fröhlich, "Fluid–particle interaction in turbulent open channel flow with fully-resolved mobile beds," Adv. Water Resour. **72**, 32–44 (2014).
[38]B. Vowinckel, T. Kempe, J. Fröhlich, and V. Nikora, "Direct numerical simulation of bed-load transport of finite-size spherical particles in a turbulent channel flow," in *Direct and Large-Eddy Simulation* (Springer, 2015), Vol. IX, pp. 663–669.
[39]B. Vowinckel, R. Jain, T. Kempe, and J. Fröhlich, "Entrainment of single particles in a turbulent open-channel flow: A numerical study," J. Hydraul. Res. **54**, 158–171 (2016).
[40]J. Jiménez, "Turbulent velocity fluctuations need not be Gaussian," J. Fluid Mech. **376**, 139–147 (1998).
[41]S. A. Morsi and A. J. Alexander, "An investigation of particle trajectories in two-phase flow systems," J. Fluid Mech. **55**, 193–208 (1972).
[42]T. R. Auton, "The lift force on a spherical body in a rotational flow," J. Fluid Mech. **183**, 199–218 (1987).
[43]S. Z. Ali and S. Dey, "Origin of the scaling laws of sediment transport," Proc. R. Soc. London, Ser. A **473**, 20160785 (2017).
[44]A. O. Celik, P. Diplas, C. L. Dancey, and M. Valyrakis, "Impulse and particle dislodgement under turbulent flow conditions," Phys. Fluids **22**, 046601 (2010).
[45]H. Reichardt, "Vollständige darstellung der turbulenten geschwindigkeitsverteilung in glatten leitungen," Z. Angew. Math. Mech. **31**, 208–219 (1951).
[46]J. Best, S. Bennett, J. Bridge, and M. Leeder, "Turbulence modulation and particle velocities over flat sand beds at low transport rates," J. Hydraul. Eng. **123**, 1118–1129 (1997).
[47]I. Nezu, "Turbulent structure in open channel flow," Ph.D. thesis, Kyoto University, Kyoto, 1977.
[48]S. K. Bose and S. Dey, "Universal probability distributions of turbulence in open channel flows," J. Hydraul. Res. **48**, 388–394 (2010).
[49]A. S. Paintal, "Concept of critical shear stress in loose boundary open channels," J. Hydraul. Res. **9**, 91–113 (1971).
[50]W. Wu, S. S. Y. Wang, and Y. Jia, "Nonuniform sediment transport in alluvial rivers," J. Hydraul. Res. **38**, 427–434 (2000).
[51]R. A. Antonia and J. D. Atkinson, "High-order moments of Reynolds shear stress fluctuations in a turbulent boundary layer," J. Fluid Mech. **58**, 581–593 (1973).
[52]M. R. Raupach, "Conditional statistics of Reynolds stress in rough-wall and smooth-wall turbulent boundary layers," J. Fluid Mech. **108**, 363–382 (1981).
[53]S. Dey, "Sediment threshold," Appl. Math. Model. **23**, 399–417 (1999).
[54]C. Hu and Q. Guo, "Near-bed sediment concentration distribution and basic probability of sediment movement," J. Hydraul. Eng. **137**, 269–275 (2011).
[55]C. H. Hu and Y. J. Hui, *Mechanics and Statistical Rule of Sediment-Laden Flow Movement in Open Channels* (Science Press, Beijing, China, 1995).
[56]T. G. Drake, R. L. Shreve, W. E. Dietrich, P. J. Whiting, and L. B. Leopold, "Bedload transport of fine gravel observed by motion-picture photography," J. Fluid Mech. **192**, 193–217 (1988).
[57]H. P. Guy, D. B. Simons, and E. V. Richardson, "Summary of alluvial channel data from flume experiments, 1956–1961," *United States Geological Survey Professional Paper, 462–I* (U.S. Dept. of Interior, Washington DC, USA, 1966).
[58]R. Fernandez Luque, "Erosion and transport of bed-load sediment," Ph.D. thesis, Delft University of Technology, Meppel, 1974.
[59]S. C. Jain, "Note on lag in bedload discharge," J. Hydraul. Eng. **118**, 904–917 (1992).
[60]A. N. Papanicolaou, "The role of turbulence on the initiation of sediment motion," Ph.D. thesis, Virginia Institute of Technology, Virginia, 1997.